Received: 15 April 2023 | Revised: 21 November 2023 | Accepted: 22 November 2023

DOI: 10.1002/mp.16880

RESEARCH ARTICLE

MEDICAL PHYSICS

# Deep-Interior: A new pathway to interior tomographic image reconstruction via a weighted backprojection and deep learning

**Chengzhu Zhang**[1] | **Guang-Hong Chen**[1,2]

[1]Department of Medical Physics, University of Wisconsin School of Medicine and Public Health, Madison, Wisconsin, USA

[2]Department of Radiology, University of Wisconsin School of Medicine and Public Health, Madison, Wisconsin, USA

**Correspondence**
Guang-Hong Chen, Department of Medical Physics and Department of Radiology, School of Medicine and Public Health, University of Wisconsin-Madison, Madison, WI, 53705, USA.
Email: gchen7@wisc.edu

**Funding information**
National Institute of Biomedical Imaging and Bioengineering, Grant/Award Numbers: R01EB032474, R01EB034011; National Heart, Lung, and Blood Institute, Grant/Award Numbers: R01HL153594, R01EB034011

## Abstract

**Background:** In recent years, deep learning strategies have been combined with either the filtered backprojection or iterative methods or the direct projection-to-image by deep learning only to reconstruct images. Some of these methods can be applied to address the interior reconstruction problems for centered regions of interest (ROIs) with fixed sizes. Developing a method to enable interior tomography with arbitrarily located ROIs with nearly arbitrary ROI sizes inside a scanning field of view (FOV) remains an open question.

**Purpose:** To develop a new pathway to enable interior tomographic reconstruction for arbitrarily located ROIs with arbitrary sizes using a single trained deep neural network model.

**Methods:** The method consists of two steps. First, an analytical weighted backprojection reconstruction algorithm was developed to perform domain transform from divergent fan-beam projection data to an intermediate image feature space, $B(\vec{x})$, for an arbitrary size ROI at an arbitrary location inside the FOV. Second, a supervised learning technique was developed to train a deep neural network architecture to perform deconvolution to obtain the true image $f(\vec{x})$ from the new feature space $B(\vec{x})$. This two-step method is referred to as Deep-Interior for convenience. Both numerical simulations and experimental studies were performed to validate the proposed Deep-Interior method.

**Results:** The results showed that ROIs as small as a diameter of 5 cm could be accurately reconstructed (similarity index $0.985 \pm 0.018$ on internal testing data and $0.940 \pm 0.025$ on external testing data) at arbitrary locations within an imaging object covering a wide variety of anatomical structures of different body parts. Besides, ROIs of arbitrary size can be reconstructed by stitching small ROIs without additional training.

**Conclusion:** The developed Deep-Interior framework can enable interior tomographic reconstruction from divergent fan-beam projections for short-scan and super-short-scan acquisitions for small ROIs (with a diameter larger than 5 cm) at an arbitrary location inside the scanning FOV with high quantitative reconstruction accuracy.

KEYWORDS
deep learning, interior tomography, image reconstruction

## 1 | INTRODUCTION

The tomographic CT image reconstruction problems using fully truncated divergent beam projection data are notoriously difficult and generally referred to as interior tomography problems.[1] In practical applications, accurate region of interest (ROI) reconstruction from fully truncated divergent beam projection data offers potential advantages in reducing the patient dose, reducing scattered radiations induced artifacts and allowing the scanning of large image objects such as obese patients. It also has the potential use for tumor visualization and dose verification in image-guided radiation therapy. However, due to the nonlocal nature of the filters used in the conventional filtered backprojection (FBP) reconstruction algorithms, a direct application of FBP reconstruction to interior tomography acquisition inevitably lead to strong truncation artifacts. Thus, it is highly desirable to investigate new pathways to address the interior tomography reconstruction problems.

If the acquired divergent beam projection data are not as fully truncated in interior tomography reconstruction problems, significant progress has been made in the past two decades with the discoveries of new analytical reconstruction schemes either in FBP or in differentiation back projection (DBP) frameworks. In particular, when the DBP framework is employed, one can focus on reconstructing image points along straight lines crossing the image object. The DBP functions along these straight lines have some profound analytical properties.[2] Using the analytical properties of the DBP functions, with some additional a priori knowledge of the interior regions, it has been proven that a stable solution exists[3–6] albeit there is no analytical solution available to perform interior tomographic reconstruction yet. But one can always reconstruct these stable ROIs using iterative image reconstruction algorithms as shown in literature.[5,7–13] Other types of a priori knowledge, such as the assumption of piecewise constant or piecewise polynomial[14] of the image objects, have also been incorporated to enable interior tomography reconstructions.[15–21] When a reliable prior image of the target image object is available, one can use the prior image constrained compressed sensing (PICCS)[22] framework to address the interior tomography reconstruction problems.[23] When the acquired divergent beam projection data are not fully truncated, analytical reconstruction or iterative reconstruction methods have been developed to reconstruct local ROIs.[2,24–28] Besides the mathematically exact methods, approximation methods can also be utilized in practice to perform good-quality local ROI reconstructions[29–31] in some applications.

In recent years, impressive advances have also been achieved in deep-learning CT reconstructions. These big-data-driven deep learning approaches offered tremendous flexibility to incorporate a priori information of the image object without needing an analytical mathematical expression. The a priori knowledge learned from a well-curated training data set can be incorporated into the image reconstructions. Specifically, the deep learning approach has been combined with either the FBP reconstruction framework or DBP reconstruction framework[32] to address many challenging reconstruction problems, such as low dose reconstruction and sparse view reconstruction problems. One can also develop an algorithm to reconstruct images directly from acquired projection data in an end-to-end trained deep neural work such as the iCT-Net proposed by the authors.[33] Some of these deep learning methods[33–37] have also demonstrated the feasibility of interior tomographic image reconstructions. However, *neither method shows that a trained deep neural network architecture could be applied to perform interior tomography reconstruction with arbitrarily selected ROI locations with consistent reconstruction accuracy*. The primary purpose of this work is to present a method to enable one trained deep neural network architecture to perform interior tomography reconstruction with arbitrary ROI locations with uniform high reconstruction accuracy, even for ROIs with diameters as small as 5.0 cm. This contrasts what has been accomplished in literature[34] that a trained deep neural network architecture was applied to the different ROI sizes with the same central location.

The new scientific contributions of this work can be summarized as follows. First, a weighted backprojection algorithm is derived to reconstruct a backprojection image, $B(\vec{x})$, which is the convolution of the target image function $f(\vec{x})$ with a shift-invariant blurring kernel $K(\vec{x}) = \frac{1}{||\vec{x}||}$, that is, $B(\vec{x}) = (f \circledast K)(\vec{x})$. Note that this result is known for parallel beam projection data with the Tuy data sufficiency condition[38–40] and the fan-beam projection data for a full scan angular range of 360°.[41] However, to the best of the authors' knowledge, similar results have not been known for either the short-scan or super-short-scan fan-beam cases. Second, a deep learning method was developed to reconstruct target images from the blurred weighted backprojection image $B(\vec{x})$. After the deep learning architecture is properly trained, the trained neural network can be applied to reconstruct the target function $f(\vec{x})$ from $B(\vec{x})$.

## 2 | WEIGHTED BACKPROJECTION IMAGE AS A CONVOLUTION BETWEEN THE TRUE IMAGE FUNCTION AND A SHIFT-INVARIANT KERNEL FOR SHORT-SCAN AND SUPER-SHORT SCAN ACQUISITIONS

### 2.1 | Mathematical notations of data acquisition geometry

Considering a 2D situation $\vec{x} = (x, y)$, suppose function $f(x, y)$ has a compact support $\mathcal{D}$, that is, $f(x, y) \equiv 0$ for

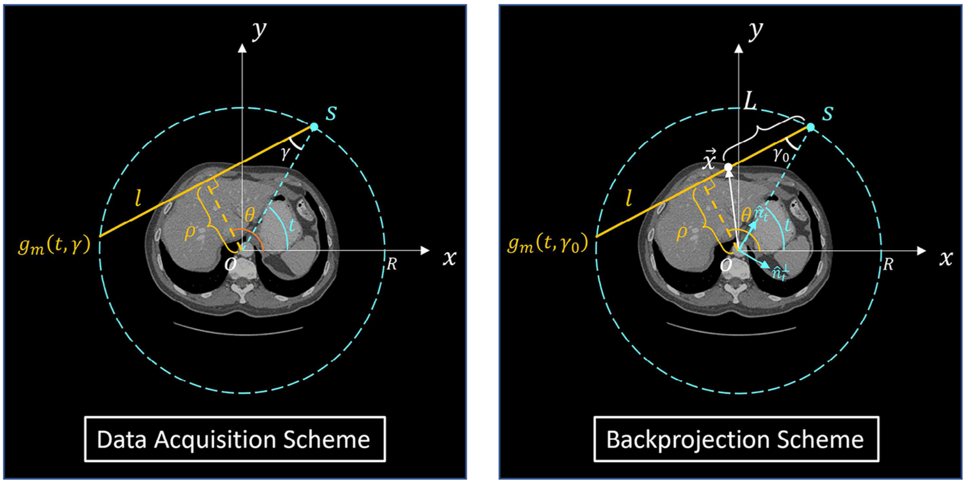

**FIGURE 1** Mathematical notations for the fan-beam CT acquisition to obtain the measured projection data $g_m(t,\gamma)$ and the corresponding parameterization in terms of $(\rho,\theta)$ (Left panel); and the corresponding backprojection to obtain $B(\vec{x})$ at a point $\vec{x}$ (Right panel). The source trajectory is circular with a radius of $R$.

$\forall(x,y) \notin \mathcal{D}$. The line integral data of function $f(x,y)$ along a straight line $\ell$ parameterized as $\ell : x\cos\theta + y\sin\theta - \rho = 0$ is given by the following integral:

$$P_\ell(\rho,\theta) = \iint_{\mathcal{D}} dxdy f(x,y)\delta(x\cos\theta + y\sin\theta - \rho), \quad (1)$$

where $\delta(\cdot)$ is the Dirac $\delta$–function in the sense of distributions. $\rho$ is the distance from the origin of the coordinate system (Figure 1) to the straight line $\ell$, and $\theta$ denotes the angle from the x-axis.

In divergent fan-beam acquisition geometry (Figure 1) with a circular trajectory with radius $R$, coordinates of the source $S$ are denoted as $(R\cos t, R\sin t)$ where $t$ is the angle from the x-axis to the iso-ray, $OS$. The same straight line $\ell$ is parameterized by the source parameter $t$ and projection angle $\gamma$, measured from the iso-ray $OS$ to the straight line $\ell$. Note that $\gamma$ is negative shown in Figure 1. The transformations between the two sets of parameters $(t,\gamma)$ and $(\rho,\theta)$ are given as below:

$$\theta = \frac{\pi}{2} + t + \gamma, \qquad \rho = -R\sin\gamma. \quad (2)$$

Similarly, if a linear detector is used, the same straight line is often parameterized by the source angle $t$ and detector coordinate $u$. In this case, all one needs to do is to define the projection angle $\gamma$ as $\gamma = \arctan\frac{u}{\mathrm{SDD}}$ in the curved detector case, where SDD is the source-to-detector distance. Note that the line integral value $P_\ell(\rho,\theta)$ does not change when the same straight line is parameterized in terms of fan-beam geometry using parameters $(t,\gamma)$. For convenience, we denote the integral value as the measured projection data $g_m(t,\gamma)$:

$$P_\ell(\rho,\theta) = g_m(t,\gamma), \quad (3)$$

for the parameter transformations shown in Equations (2).

## 2.2 | Direct backprojection from parallel-beam acquisition geometry and generalization to the full-scan fan-beam acquisitions

In preparation for a comparison between widely recognized results in literature and our findings to be discussed in the subsequent subsection, we begin by defining the direct backprojection image $B_\parallel(\vec{x})$ using the parallel-beam projection data as represented in Equation (1):

$$\begin{aligned}
B_\parallel(x,y) &= \int_0^\pi d\theta P_\ell(\rho,\theta)|_{\rho=x\cos\theta+y\sin\theta}, \\
&= \iint dx'dy' f(x',y') \int_0^\pi d\theta\delta[(x'-x)\cos\theta + (y'-y)\sin\theta], \\
&= \iint dx'dy' f(x',y') \frac{1}{\sqrt{(x-x')^2+(y-y')^2}}, \\
&= f(x,y) \circledast \frac{1}{\sqrt{x^2+y^2}}. \qquad (4)
\end{aligned}$$

This equation represents classical results initially discovered by Bates[38] in 1971, subsequently included in standard textbooks.[39,40] Specifically, it elaborates that the direct backprojection of the obtained parallel-beam projection data defined in Equation (1) using the direct backprojection defined in Equation (4) results in a backprojection image equivalent to the convolution of the true image $f(x,y)$ with a two-dimensional one-over-distance kernel.

Using the same direct backprojection defined in Equation (4), Gullberg[41] showed that the direct backprojection of fan-beam projection data acquired over a $2\pi$ angular range:

$$B_{2\pi}(\vec{x}) = \frac{1}{2}\int_0^{2\pi} dt\, g_m(t,\gamma)|_{\gamma=\gamma_0(\vec{x},t)}, \tag{5}$$

can also be shown to be equal to the convolution between the true image function $f(x,y)$ and the one-over-distance 2D filter:

$$B_{2\pi}(\vec{x}) = f(x,y) \circledast \frac{1}{\sqrt{x^2+y^2}} \tag{6}$$

The factor of $\frac{1}{2}$ introduced in Equation (5) accounts for the data redundancy in full scan acquisitions. To the authors' best knowledge, over the past four decades, Gullberg's results for full-scan fan-beam acquisitions have not been extended to scenarios where the angular scan range is less than $2\pi$. We present a detailed derivation of the above findings in Appendix C. Our derivations unequivocally reveal that the aforementioned results (Equation (5) and Equation (6)) for the full-scan fan-beam data acquisition arise from a unique geometrical identity. Importantly, this identity holds true only for full scan acquisitions and is not applicable when the scan's angular range is shorter than $2\pi$. This provides a clear explanation for why the aforementioned result has not been successfully extended to scenarios where the angular scan range is less than $2\pi$.

## 2.3 | A weighted backprojection scheme to enable the generalization of result shown in Equation (6) to the cases with an angular scan range shorter than $2\pi$

In this subsection, we demonstrate that with a weighted backprojection approach, the findings presented in Equation (4) for parallel-beam acquisitions and Equation (6) for full-scan fan-beam acquisitions can be extended to encompass any fan-beam data acquisition angular scan range and to the interior-tomography case.

Suppose $\Gamma_{\vec{x}}$ is any scanning arc satisfying the Tuy data sufficiency condition.[42] We define a weighted backprojection image $B(\vec{x})$ that can be computed from the measured projection data in a fan-beam geometry with a curved detector geometry as follows:

$$B(\vec{x}) = \int_0^{\Gamma_{\vec{x}}} dt \frac{R\omega(t,\gamma)\cos\gamma}{L(\vec{x},t)} g_m(t,\gamma)|_{\gamma=\gamma_0(t,\vec{x})}, \tag{7}$$

$$L(\vec{x},t) = \sqrt{(x-R\cos t)^2+(y-R\sin t)^2}, \tag{8}$$

$$\gamma_0(\vec{x},t) = \arctan\frac{\vec{x}\cdot\hat{n}_t^{\perp}}{R-\vec{x}\cdot\hat{n}_t}. \tag{9}$$

where $\hat{n}_t = (\cos t, \sin t)$ and $\hat{n}_t^{\perp} = (\sin t, -\cos t)$ are two mutually perpendicular unit vectors associated with source locations. $\gamma_0(\vec{x},t)$ is the projection angle from the source location to the reconstruction point $\vec{x}$ and $L(\vec{x},t)$ is the distance from the image point $\vec{x}$ to the source location $(R\cos t, R\sin t)$ as shown in Figure 1. $\omega(t,\gamma)$ is a normalized weighting factor for data redundancy. For example, $\omega = \frac{1}{2}$ for redundant measurements and 1 for non-redundant measurements, but other smooth weight factors are also good choices such as the Parker weighting scheme, which was adopted for short-scan and super-short-scan data reconstruction in this work.

To underscore the main innovation of this work, one should compare the definition of the backprojection image $B(\vec{x})$ as given by Equation (7) with the direct projection approach articulated in Equations (5) and (6) which represents the Gullberg scheme for full-scan fan-beam acquisitions and Equation (4) that pertains to the well-known parallel-beam acquisitions. The crucial distinction is encapsulated by the weighting factor:

$$\frac{R\omega(t,\gamma)\cos\gamma}{L(\vec{x},t)} \tag{10}$$

in our proposed backprojection method. This weighting factor encompasses not just a data redundancy factor $\omega(t,\gamma)$, which intuitively reduces to $\frac{1}{2}$ for the full-scan scenario, but also incorporates a geometrical factor $\frac{R\cos\gamma}{L(\vec{x},t)} = \frac{1}{2}\frac{2R\cos\gamma}{L(\vec{x},t)}$. Since $2R\cos\gamma$ represents the total length of the chord along the direction from the source to the backprojection point $\vec{x}$, as shown in Figure 1, the weighting function is one half of the ratio of the total chord length to the distance from the source to the backprojection point. A shorter distance from the source to the backprojection points corresponds to a higher assigned weight. In conclusion, this factor ensures a delicately tailored weight is assigned to the backprojection image point based on the distance $L(\vec{x},t)$ between the backprojection point $\vec{x}$ and the source position.

When the reconstruction task is for an ROI, then the above backprojection operation should be defined over an angular range $\Gamma = \cup_{\vec{x}\in \mathrm{ROI}}\Gamma_{\vec{x}}$, that is, the union of the angular range for each of the point inside the ROI. For simplicity, the subscript $\vec{x}$ in $\Gamma_{\vec{x}}$ will be omitted in the remainder of the paper whenever there is no confusion in understanding.

Since only the projection data from those rays passing through the target ROI are used in the reconstruction of the backprojection image $B(\vec{x})$, it is clear that the x-ray beam can be collimated only to illuminate the target ROI regardless of whether the projection data outside the ROI are measured or not. This is to say that this is an interior tomography data acquisition provided that the target ROI only consists of the interior points of the function support $\mathcal{D}$.

Using the innovative definition of the backprojection image presented in Equation (7), we can derive the following theorem, as elaborated in Appendix A:

**Theorem.** *The backprojection image* $B(\vec{x})$ *defined in Equation (7) is a blurred version of the original image* $f(\vec{x})$ *in an image support* $\mathcal{D}$ *with a shift-invariant blurring kernel* $K(\vec{x}) = \frac{1}{||\vec{x}||} = \frac{1}{\sqrt{x^2+y^2}}$, *that is,*

$$B(\vec{x}) = (f \circledast K)(\vec{x}) = \iint_{\mathcal{D}} d^2\vec{x}_0 \frac{f(\vec{x}_0)}{||\vec{x}_0 - \vec{x}||}. \tag{11}$$

*provided that backprojection angular ranges in Equation (7) for a target ROI satisfy the Tuy data sufficiency condition. While the content on the right-hand side of the aforementioned equation happens to be the same as the well-established parallel-beam results and the findings by Gullberg for the full-scan fan-beam acquisition, but this is not the key point. Instead, the key point is the method to reconstruct* $B(\vec{x})$ *from the measured projection data. As it is explicitly shown in Equation (7), the method of generating the backprojection image* $B(\vec{x})$ *in our work is totally different from the direct backprojection methods previously introduced in the literature.*

## 2.4 | Image reconstruction from the weighted backprojection by deep learning

### 2.4.1 | Image reconstruction from the weighted backprojection image: Direct reconstruction methods

When the weighted backprojection image $B(\vec{x})$ is computed from non-truncated projection data, one can use the convolution property to obtain the Fourier transform, $\tilde{f}(\vec{\xi})$, of the image function $f(\vec{x})$ as follows:

$$\tilde{f}(\vec{\xi}) = ||\vec{\xi}||\mathbf{F}[B](\vec{\xi}), \tag{12}$$

where $\mathbf{F}[B](\vec{\xi})$ is the Fourier transform of the backprojection image $B(\vec{x})$, and $\vec{\xi} = (\xi_x, \xi_y)$ are the spatial frequency vector. In principle, an inverse Fourier transform can then be taken to reconstruct the image function $f(\vec{x})$:

$$f(\vec{x}) = \mathbf{F}^{-1}[||\vec{\xi}||\mathbf{F}[B](\vec{\xi})](\vec{x}). \tag{13}$$

However, it is challenging to numerically implement the above inverse Fourier transform because the backprojection image $B(\vec{x})$ is not compactly supported, or equivalently, the Fourier transform $\mathbf{F}[B](\vec{\xi})$ is not bandlimited. This is one of the key reasons that the above $B(\vec{x})$-based reconstruction algorithm was not extensively studied in the past. It is even more problematic when $B(\vec{x})$ is further truncated to a small ROI due to data truncation.

Alternatively, one can also search for an approximation $\hat{f}(\vec{x})$ of the image function $f(\vec{x})$ within an ROI by solving the following regularized deconvolution optimization problem:

$$\hat{f}(\vec{x}) =: \min_U \left[\frac{1}{2}||K \circledast U - B||^2_\Omega + \lambda R(U)\right], \tag{14}$$

where $R(U)$ is the so-called regularizer or prior of the function $U(\vec{x}) \in \Omega$ in the sense of Bayesian inference, $\Omega$ is a functional space with proper norm defined, and $\lambda$ is a hyper-parameter to control the tradeoff between the data fidelity encoded in Equation (11) and the regularizer $R(U)$. However, identifying a suitable regularizer (i.e., $R(U)$) for interior tomographic reconstruction problems remains a challenging task.

### 2.4.2 | Proposed Deep-Interior reconstruction strategy

With the recent rise of deep learning studies, we are offered a new computational platform to relax the need to handcraft regularizers in the above deconvolution reconstruction process. When a large amount of well-curated training data pairs $\{(B_i(\vec{x}), f_i(\vec{x}))\}_{i=1}^S$ are available, where $B_i(\vec{x})$ is the blurred image of $f_i(\vec{x})$ and the training data set has a sample size of $S$, these training pairs can be used to learn a feedforward convolutional neural network, $\mathbf{D}$, to directly map the blurred input image $B_j(\vec{x})$ to the desired image function $f_j(\vec{x})$ as its output. Namely,

$$f_j(\vec{x}) = \mathbf{D}(\mathbf{M}B_j(\vec{x})), \tag{15}$$

where $\mathbf{M}B(\vec{x})$ is the cropped image that is consistent with an interior tomography data acquisition with narrowly collimated x-ray beams, and this beam collimation and image cropping operation is modeled by the introduced mask operator $\mathbf{M}$, determined by the data acquisition. Preliminary studies[43] demonstrated this deep learning scheme is feasible when data are not truncated. However, it is unclear how a trained deep neural network $\mathbf{D}$ can yield accurate reconstruction as the beam collimation decreases. Mathematically speaking, when the beam collimation is reduced, the data available in the data fidelity term in Equation (14) also decreases, and the ill-posedness of the problem is more and more severe.

In this work, the feedforward deep neural network architecture $\mathbf{D}$ is trained by solving the following optimization problem using the backpropagation

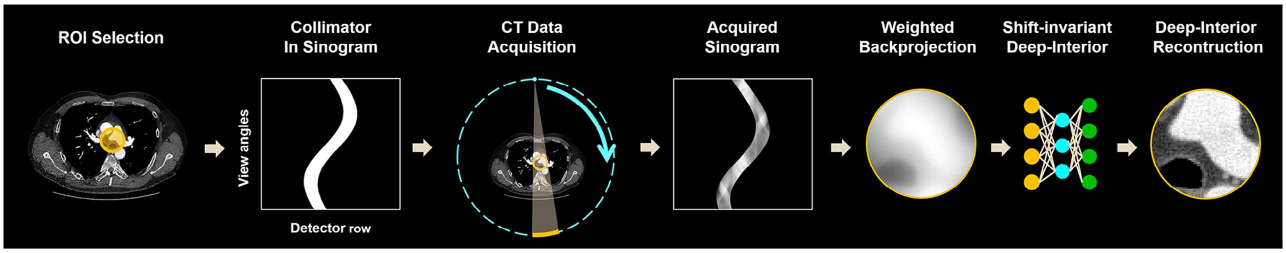

**FIGURE 2** Workflow of the proposed Deep-Interior reconstruction pipeline. The second figure from the left shows the collimation in sinogram for minimally needed data acquisition for an ROI. The third figure demonstrated the x-ray illumination of a patient to acquire a $\phi = 5$ cm ROI represented by a yellow circle. The $B(\vec{x})$ image of the ROI region can then be accurately acquired through backprojection. The trained network is then used to reconstruct the ROI. ROI, regions of interest.

algorithm:

$$\hat{\mathbf{D}} = \min_{\mathbf{D}} \sum_{i=1}^{S} \|\mathbf{DM}B_i - f_i\|_1, \qquad (16)$$

Once the network is trained, the shift-invariant nature of the blurring kernel dictates that the trained network **D** can be readily applied to ROIs regardless of their locations in a field of view. This means the ROI to be reconstructed does not have to be centered on the iso-center of the rotating gantry, as required in Ref. [34].

## 3 | MATERIALS AND METHOD

### 3.1 | Workflow and deep neural network architecture of the proposed Deep-Interior reconstruction strategy

Figure 2 presents the proposed Deep-Interior reconstruction workflow. The widely known U-Net[44] was used as the deep neural network architecture to implement the proposed reconstruction framework. Detailed network specifications are presented in Figure 3. $C$ denotes the starting number of channels, and $N$ relates to the input image dimension. This work empirically selects the number of channels as $C = 64$ and $N = 4$ for $\phi = 5.0$ cm. As a result, the total trainable parameters are roughly 22 million. In principle, any modified or more sophisticated neural network architecture can replace the U-Net backbone used in this work. The choice of U-Net demonstrated that the base network was sufficient to learn a generalizable deconvolution scheme for ROIs at an arbitrary location.

### 3.2 | Curation of training, validation, and testing data sets

**TABLE 1** The numerical dataset partition for training, validation, and testing.

| | Training | Validation | Testing |
|---|---|---|---|
| **Chest CT** | 1905 | 112 | 224 |
| **Abdominal CT** | 1792 | 175 | 560 |
| **Head CT** | 1712 | 128 | 283 |

A numerical training dataset is carefully curated to train such a small FOV reconstruction network. The reconstructed ROI can be either a circular FOV or a square FOV cropped from a slightly larger circular FOV. This work mainly showed our Deep-Interior reconstruction results using a circular FOV. The training dataset was generated from clinical CT images by numerical simulations without adding noise. The images covered various anatomical structures, for example, head, chest, upper abdomen, lower abdomen, and pelvis. Each slice was a $512 \times 512$ matrix and treated as an image with a $\phi = 40.0$ cm diameter. The data partition is exhibited in the following table.

A standard ray-driven forward projection procedure was performed to acquire the numerical sinogram data specific to each ROI. The parameters for the fan-beam acquisition geometry are the same as that used in Discovery 750 HD (GE Healthcare, WI, USA). The x-ray illumination was collimated to a given ROI with minimally needed view angles satisfying Tuy data sufficiency. The unilluminated part of the detector was set to zero. A weighted backprojection with Parker weighting was performed to obtain a $B(\vec{x})$ image from each sinogram data. These backprojection images were normalized to [0, 1]. The reference image for each ROI image was cropped from the ground truth image. Ground truth was used for quantitative comparison purposes.

The training data were prepared by selecting equally-spaced ROIs with a stride of 2.5 cm (32 pixels), and 612 995 training data pairs were collected to train the Deep-Interior network. Note also that the test data were selected from completely different patient cases not used for the network training. The details of data used in training, validation, and testing are provided in Table 1 and Table 2.

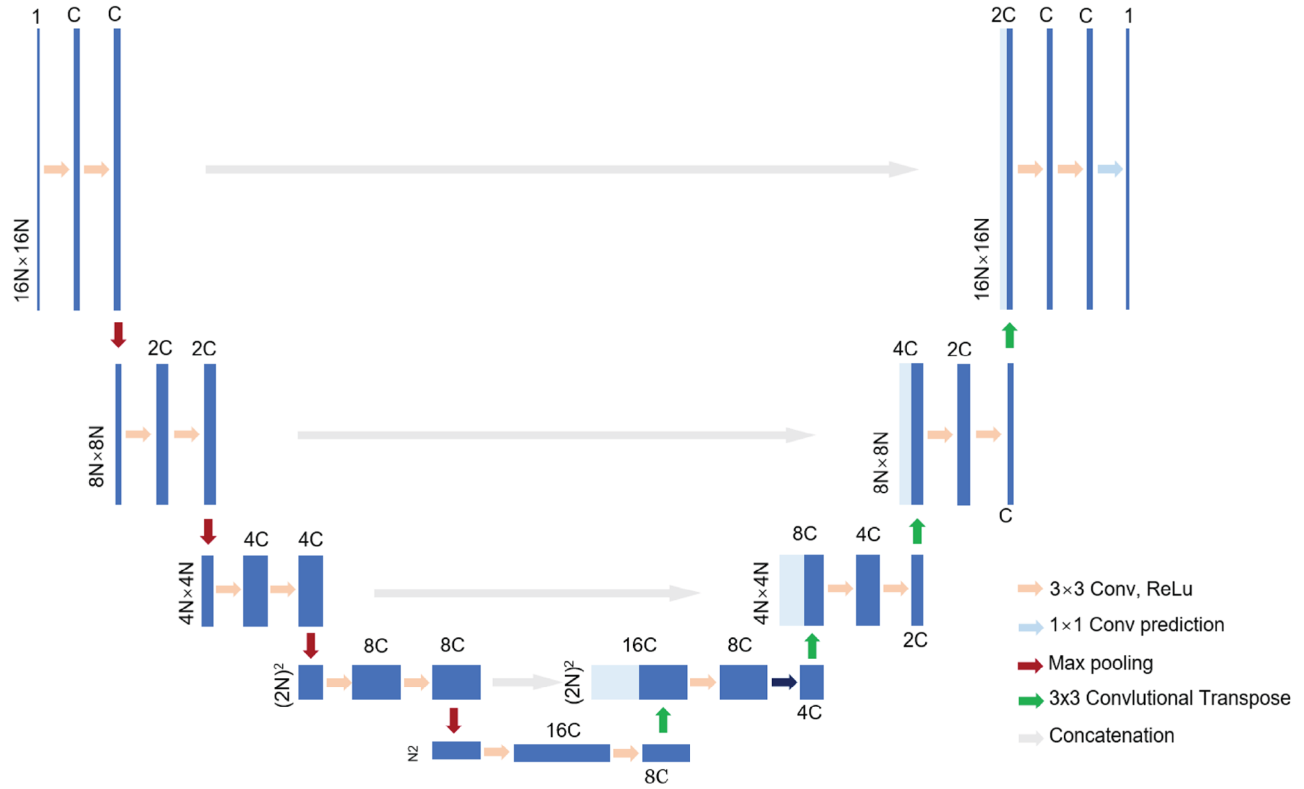

**FIGURE 3** The figure exhibits the network architecture of U-Net employed in this work. Specifically, a four-pooling-layer U-Net consists of four stages connected by 2 × 2 max-pooling layers (Pooling) in the first half and convolution-transpose layers (ConvTranspose) in the second half. Each stage has two groups: a 3 × 3 convolution layer (Conv), a batch-normalization layer (Bnorm), and a ReLu layer. The number of channels for each convolution layer is doubled after each pooling layer. A scale-by-scale concatenation strategy is leveraged after each ConvTranspose layer to incorporate the higher-resolution structural information from previous stages. *C* denotes the starting number of channels, and *N* relates to the input image dimension.

**TABLE 2** The numerical dataset partition for training, validation, and testing.

| | Training | Validation | Testing |
|---|---|---|---|
| **Chest CT** | 1905 | 112 | 224 |
| **Abdominal CT** | 1792 | 175 | 560 |
| **Head CT** | 1712 | 128 | 283 |

## 3.3 | Network training specifics

The network training was performed on a workstation with a graphic processing unit (GPU) (Nvidia GTX 1080Ti). The network was trained using an Adam optimizer ($\beta = 0.5$) with a mean absolute difference loss function. No additional regularizer was added to the loss function. For numerical data training, the initial learning rate was $1 \times 10^{-4}$ and gradually decreased every 20 epochs with a decay factor of 0.5. The maximum training epochs were set to 100, resulting in the minimum learning rate of $6.25 \times 10^{-6}$. The moving average of the validation loss was monitored to avoid overfitting. The training took one day. During the testing phase, it took 0.01 second to reconstruct one ROI.

## 3.4 | Generalizability test: From trained Deep-Interior model using numerical simulation data to experimental dataset

The generalizability of the trained network was investigated by testing its performance on the external experimental dataset. Specifically, the deep neural network $\hat{\mathbf{D}}$ trained by the numerical simulation data was directly applied, that is, without any fine-tuning process, to reconstruct images using the weighted backprojection images $B(\vec{x})$ reconstructed from the experimental sinogram data.

With HIPAA compliance and IRB approval, raw sinogram datasets of 77 human subjects (376 slices) scanned with a coronary CT angiography protocol were retrospectively retrieved. The step-and-shoot short-scan acquisition mode acquired the projection data on a 64-slice CT scanner (Discovery CT 750HD, GE Healthcare) with a 100 or 120 kV tube potential and milliampere ranging from 270 to 800 mA. A number of 376 test image slices and the corresponding sinogram projection data were collected for this work.

To generate reference images for performance quantification, the conventional non-truncated short-scan

FBP reconstruction was performed to reconstruct image slices with a FOV of $\phi = 40$ cm without truncation, image size of $512 \times 512$, slice thickness of 3.75 mm. It is worth noting that due to the data acquisition and reconstruction process, FBP as the reference image is a slightly blurred version of the ground truth image in numerical studies. Thus residual edges are expected in the difference image when comparing the trained Deep-Interior to the reference image.

## 3.5 | Quantitative quality evaluation metrics

Reconstruction accuracy is quantified using two standard metrics: relative root mean square error (rRMSE) and structural similarity index metric (SSIM), defined as follows:

$$\mathrm{rRMSE}(\vec{x}, \vec{x}_0) = \frac{||\vec{x} - \vec{x}_0||_2}{||\vec{x}_0||_2} \times 100\%, \tag{17}$$

where $\vec{x}$ denotes the vector form of the reconstructed image, $\vec{x}_0$ denotes the vector form of the ground truth or reference image.

$$\mathrm{SSIM}(\mathbf{x}, \mathbf{x}_0) = \frac{(2\mu_{\mathbf{x}}\mu_{\mathbf{x}_0} + a_1)(2\sigma_{\mathbf{x},\mathbf{x}_0} + a_2)}{(\mu_{\mathbf{x}}^2 + \mu_{\mathbf{x}_0}^2 + a_1)(\sigma_{\mathbf{x}}^2 + \sigma_{\mathbf{x}_0}^2 + a_2)}, \tag{18}$$

where $\mu_{\mathbf{x}}$ denotes the mean value of image $\mathbf{x}$, $\sigma_{\mathbf{x}}$ denotes the variance of $\mathbf{x}$, and similar properties are defined for the reference image $\mathbf{x}_0$. $\sigma_{\mathbf{x},\mathbf{x}_0}$ denotes the cross-covariance of $\mathbf{x}$ and $\mathbf{x}_0$. $a_1 = 1 \times 10^{-6}$ and $a_2 = 3 \times 10^{-6}$ are two constants chosen based on the dynamic range of CT images [0, 0.1] mm$^{-1}$ and are used to stabilize the division with a small denominator. Notice that SSIM was calculated locally for a given pixel and should be denoted as $\mathrm{SSIM}(\mathbf{x}, \mathbf{x}_0, l)$ at location $l$. An overall SSIM value was calculated by averaging over all locations of a reconstructed ROI image to represent the reconstruction accuracy.

Note that these metrics quantified all reconstructed images by excluding the area outside the circular FOV.

# 4 | RESULTS

In this section, results are presented to demonstrate the reconstruction accuracy of the weighted backprojection image $B(\vec{x})$ using the reconstruction formula Equation (7). Followed by that are the results demonstrating the reconstruction accuracy of the proposed Deep-Interior method.

## 4.1 | Reconstruction accuracy of the weighted backprojection images for short-scan and super-short-scan acquisitions

To validate the reconstruction formula shown in Equation (7), reference images used in numerical simulations to generate training data were numerically blurred by the kernel $K(\vec{x})$ as shown in Equation (11). The blurring was achieved by forward projection followed by an unweighted backprojection in parallel-beam geometry. The difference images between the reconstructed $B(\vec{x})$ using Equation (7) and the blurred version using Equation (11) were generated. The corresponding rRMSEs were calculated.

As shown in Figure 4, we have studied both the conventional direct backprojection and the proposed weighted backprojection, as described in Equation (7). Backprojection images have been reconstructed for full-scan ($\Gamma = [0, 2\pi)$), short-scan ($\Gamma = [0, \pi + \gamma_m)$), and super-short-scan($\Gamma = [0, \pi)$) data, and subsequently compared with reference images. $\gamma_m$ denotes the fan angle of the CT scanner (Discovery CT 750HD, GE Healthcare), which is about 60°. The error images and the reconstruction errors, when evaluated using rRMSE and excluding areas outside the phantom, reveal minimal discrepancies for the proposed method across all data acquisition scenarios. In contrast, the direct backprojection method is only suited for the full-scan case.

## 4.2 | Deep-Interior: Shift-invariant reconstruction performance at arbitrary ROI locations and arbitrary anatomical sites

A trained Deep-Interior neural network model was applied to the test data sets with small ROIs with a diameter of $\phi = 5.0$ cm. These ROIs are located at arbitrary locations and three different anatomical sites (chest, abdomen, and pelvis). The Deep-Interior neural network model does not see these test data sets in training. For the numerical test dataset, the trained Deep-Interior deep neural network can reconstruct all small ROIs with high reconstruction accuracy in terms of rRMSE ($2.4 \pm 1.1\%$) and similarity indices SSIM ($0.985 \pm 0.018$). Figure 5 demonstrates three reconstructed images of different anatomical structures: (a) chest, (b) abdomen, and (c) pelvis. The results of five ROIs marked by circles are displayed correspondingly on the right side of the image. Specifically, the $B(\vec{x})$ image, the FBP image

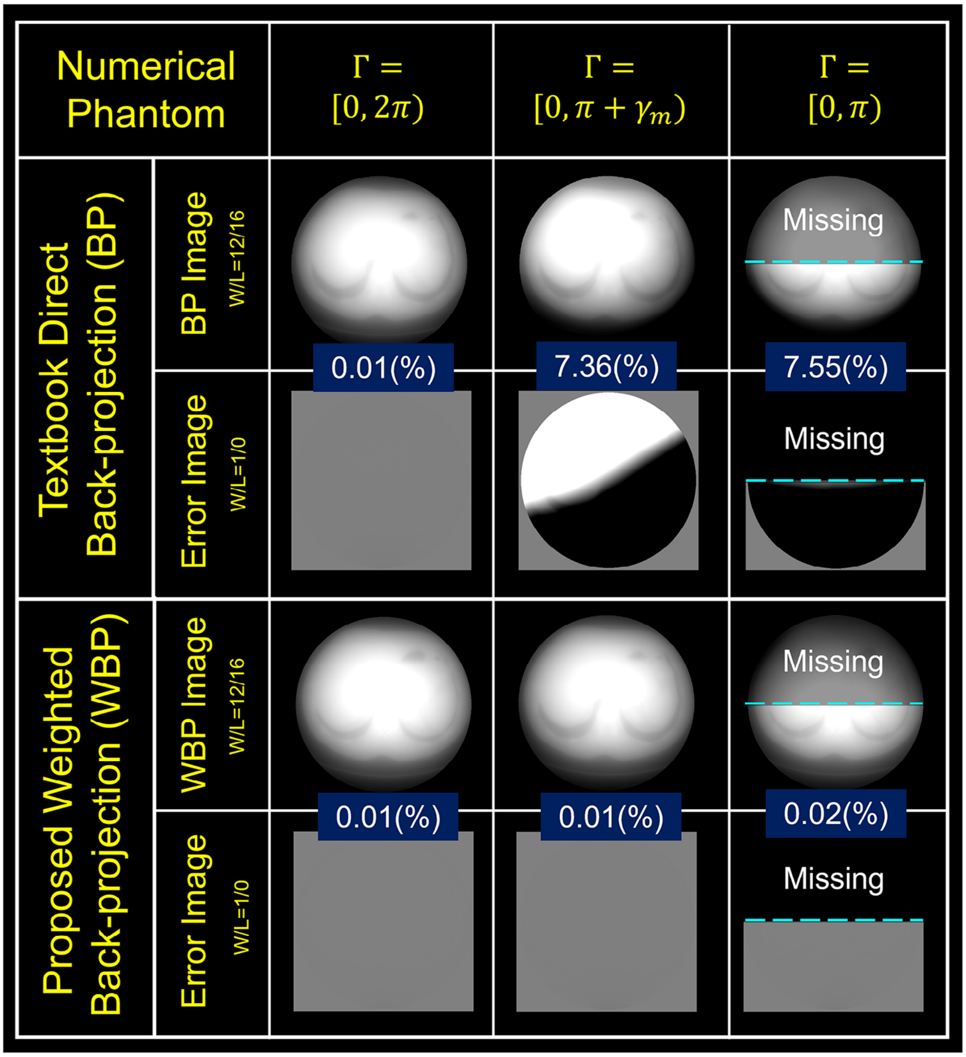

**FIGURE 4** Comparison between the conventional direct backprojection and our proposed weighted backprojection method is conducted using a numerical abdominal phantom. The conventional direct backprojection is illustrated in the top row, while the proposed weighted backprojection approach is exhibited in the second row. Evaluations span across various data acquisition scenarios: (1) Full scan ($\Gamma = [0, 2\pi)$), (2) Short-scan ($\Gamma = [0, \pi + \gamma_m)$), and 3. Super-short-scan ($\Gamma = [0, \pi)$) data. $\gamma_m \approx 60°$ denotes the fan angle of the CT scanner. Note that, for the super-short-scan data, the segment illustrating missing data in the reconstructed image is marked above the dashed line. All analyses, both visual and quantitative, are centered on the region below the dashed line, encapsulating areas with sufficient data. Note that the gray color represents a zero difference while bright and dark colors represent large differences.

reconstructed by applying the standard FBP algorithm to the truncated data (Truncated FBP), the reconstructed ROIs from the $B(\vec{x})$ image using the trained Deep-Interior network (Deep-Interior), the ground truth image (Ref), and their difference images (Diff) are shown from left to right. rRMSE and SSIM results corresponded to the Deep-Interior image when compared to the ground truth image. The reconstructed ROIs cover a variety of low-contrast, high-contrast, and uniform anatomical structures such as contrast-enhanced heart ventricles, spines, hepatic veins, spleen, colons, bone, bone spongiosa, and so on. The selected positions also range from the patient's center to peripheral bodies. We also note that no selected ROI locations in these images were included in the training process.

## 4.3 | Deep-Interior: Generalizability test of the trained network model to experimental human subject data

To assess whether the Deep-Interior reconstruction model truly learned to perform the desired two-dimensional deconvolution from the reconstructed $B(\vec{x})$ without dependence on the training data set, which was numerically generated, we directly applied the trained Deep-Interior model to the reconstructed $B(\vec{x})$ from the

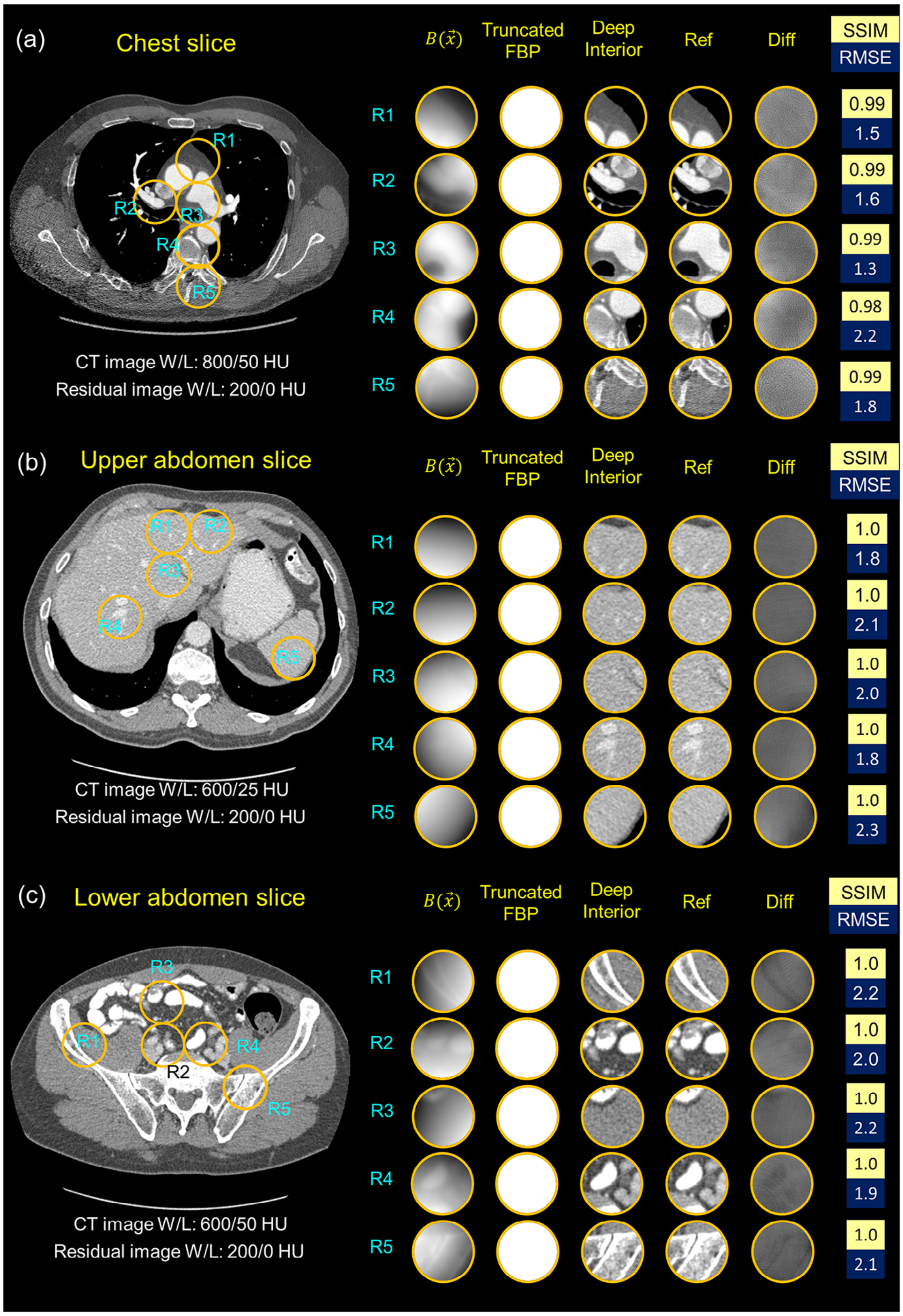

**FIGURE 5** Reconstruction accuracy assessment of the trained Deep-Interior network model. The model was applied to numerically generated test data (detailed in Section 3.2) for three different anatomical sites: (a) a chest slice, (b) an upper abdomen (liver) slice, and (c) a lower abdomen (pelvis) slice. For each site, five ROIs were designated to quantify the reconstruction accuracy. Display windows for the difference images are set at W/L=200/0 HU. The CT image display windows are: (a) chest W/L=800/50 HU, (b) abdomen W/L=600/25 HU, and (c) pelvis W/L=600/50 HU.

sinogram projection data of the CT scanner. Namely, the acquired full FOV sinogram projection data is retrospectively collimated to conformally cover the selected ROIs as shown in Figure 6 to simulate actual interior tomographic data acquisitions. Using the truncated sinogram for each marked ROI, the weighted backprojection images $B(\vec{x})$ were reconstructed using Equation (7). These reconstructed backprojection images are fed into the trained Deep-Interior neural network model to reconstruct the ultimate ROIs. The reconstruction accuracy is

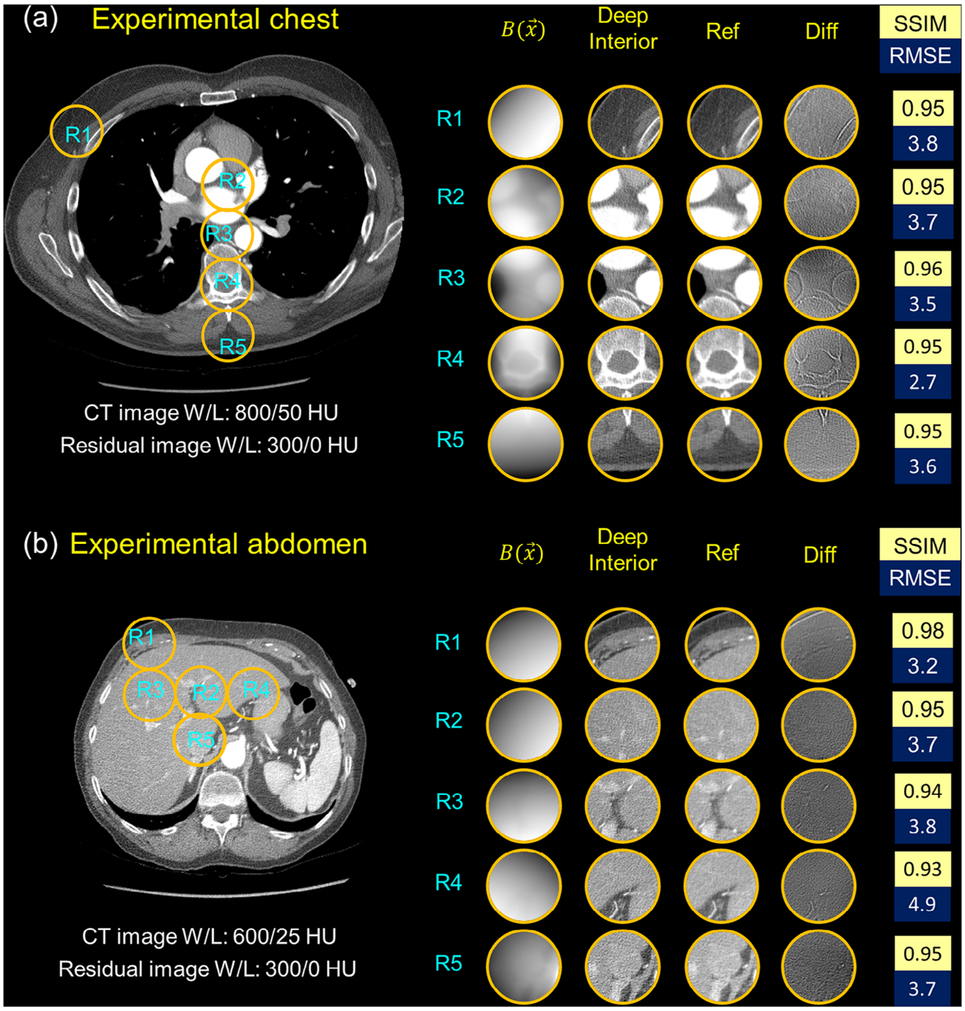

**FIGURE 6** Deep-Interior reconstruction using experimental projection data (FOV size: $\phi = 5.0$ cm). (a) Chest and (b) Abdomen. Display windows: Chest W/L=800/50 HU; Abdomen W/L=600/20 HU; WL=300/0 HU for all difference images.

evaluated using the SSIM metric. SSIM was reported at $0.940 \pm 0.025$ across the entire human subject test dataset. The results showed remarkable reconstruction accuracy with 0.93 better SSIM than the reference image reconstructed from full FOV data using FBP for the same ROIs.

## 4.4 | Deep-Interior: To reconstruct arbitrary size ROIs using a single trained deep neural network model

The shift-invariant reconstruction performance of the trained Deep-Interior network naturally enables ROI reconstruction of arbitrary sizes. As a proof of concept, reconstructed circular ROIs of diameter $\phi = 5$ cm at different positions were assembled to form a larger circular ROI without additional training of a different network. One of the straightforward stitching schemes to form a larger ROI, for example, $\phi = 10$ cm, is shown in Figure 7: several small ROIs were stitched and then cropped to a circular FOV for visualization. Figure 7 further shows an example of reconstructing multiple ROIs of different sizes using experimental projection data retrospectively collimated to the corresponding assembly of small ROIs. Their quantitative evaluation of reconstruction accuracy compared to non-truncated FBP (Ref) is exhibited.

## 4.5 | Deep-Interior: Reconstructing cone-Beam data by projecting 3D slices onto 2D slices

In contemporary medical imaging, for a range of practical applications, one can employ the Feldkamp approximation[45] to extend the use of our Deep-interior reconstruction method to cone-beam CT acquisitions when the cone angle is relatively small. This extension is achieved by incorporating an additional weighting step into the Deep-Interior setup. In order to enable volume-of-interest (VOI) reconstruction for cone-beam CT, we

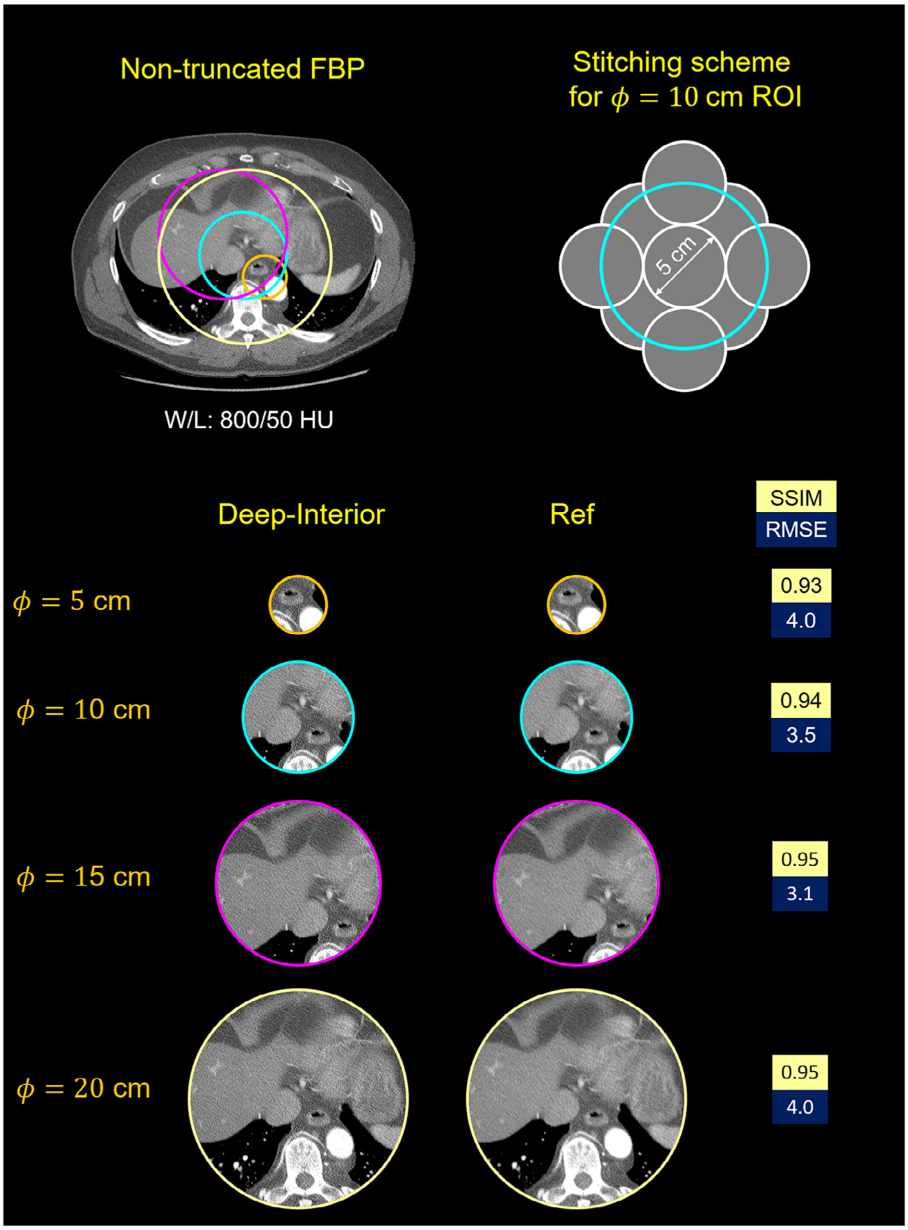

**FIGURE 7** An example of reconstructing ROIs of different sizes for a single image using the trained Deep-Interior network for circular FOV with diameter $\phi = 5$ cm. The exemplary stitching scheme is shown for a larger ROI with diameter $\phi = 10$ cm. Four sizes were shown with diameters of 5, 10, 15, and 20 cm. SSIM and rRMSE comparing Deep-Interior to non-truncated FBP are shown as well. The window levels are W/L=800/50 HU for CT images. FOV, field of view; rRMSE, relative root mean square error; ROI, regions of interest; SSIM, structural similarity index metric.

project data from various rows of the multi-row detector onto the scanning plane, utilizing a cosine factor. For a cylindrical detector, this cosine factor is expressed as:

$$\cos\tau = \frac{\text{SDD}}{\sqrt{\text{SDD}^2 + v^2}} \tag{19}$$

In this equation, SDD signifies the distance from the source to the detector, and $v$ represents the height of the detector row. By leveraging this weighting factor, the projection data obtained can be backprojected into the feature space $B(\vec{x})$, row-by-row, mirroring the FDK algorithm's approach. Following this, the previously trained deconvolution network is applied to each slice of $B(\vec{x})$. Benefiting from batch processing, this approach facilitates efficient 3D image reconstruction, addressing concerns related to processing time. Figure 8 presents the deep-interior for the experimental testing cone-beam CT cases described in Section 3.4 over three different representative VOIs.

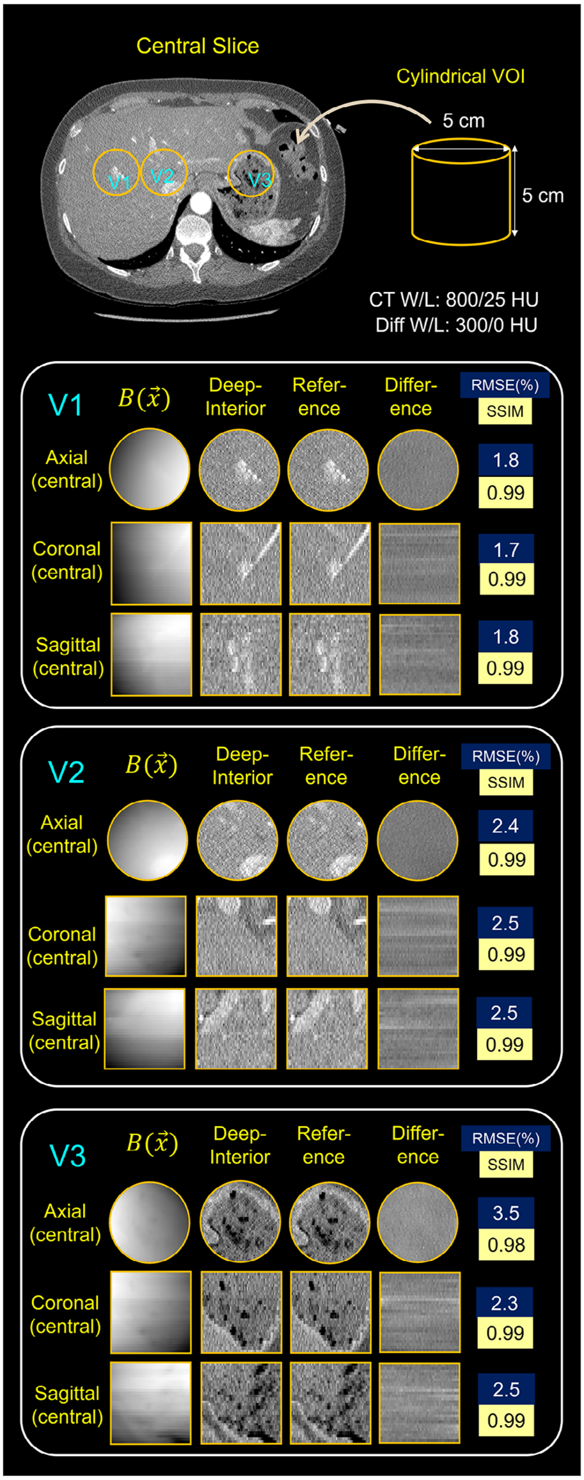

**FIGURE 8** Deep-Interior reconstructs cylindrical VOIs of dimensions $64 \times 64 \times 32$ pixels, equivalent to a spatial size of $5 \times 5 \times 5$ cm$^3$, using experimental cone-beam data. The illustrations showcase three VOIs in central axial, coronal, and sagittal slices. Reconstructions include the weighted backprojection image $B(\vec{x})$, Deep-Interior's results, and reference FBP images. The reconstruction differences between Deep-Interior and the reference images are quantified using rRMSE (%) and SSIM metrics. The window levels are W/L=800/25 HU for CT images and 300/0 HU for difference images. FBP, filtered backprojection; rRMSE, relative root mean square error; SSIM, structural similarity index metric; VOI, volume-of-interest.

## 5 | DISCUSSION

This paper developed and validated a new image reconstruction framework to address the interior tomographic reconstruction problem. In this framework, the proposed image reconstruction formula (Equation (7)) was used to reconstruct the weighted backprojection image $B(\vec{x})$ from the measured fan-beam projection data. It is remarkable to show that this backprojection image is the blurred version of the actual image $f(\vec{x})$ by a shift-invariant kernel $K(\vec{x}) = \frac{1}{||\vec{x}||}$ and this is true for arbitrary ROIs using the data acquired in the corresponding view angle range satisfying the Tuy data sufficiency condition. The reconstructed backprojection images are then de-convolved to reconstruct the desired interior tomographic images using a single trained deep neural work model. The same trained model from numerical simulations was also directly applied to experimental human subject data without fine-tuning to show remarkable reconstruction accuracy. This indicates that the trained model indeed learned to perform the desired deconvolutions to unwrap the effect of the shift-invariant blurring kernel $K(\vec{x})$. If one wants to reconstruct large-size ROIs, the reconstructed small ROIs can be stitched together without using new neural network models. Compared to state-of-the-art method, Deep-Interior is unique to reconstructing small ROIs at arbitrary location and with arbitrary sizes. However, we acknowledge that it has not been equipped with low-dose,[35] undersampling[34] and exterior estimation[36] capabilities which are available in literature.

Several potential limitations in this work should be addressed in future works: (1) Systematic investigations need to be performed to study the breakdown limit of the ROI sizes. When the beam is collimated from smaller and smaller ROI sizes, the ill-posedness of the deconvolution problem becomes more severe. It would be interesting to see how much deep learning strategy can be further leveraged to address this more challenging deconvolution problem. (2) Systematic investigations are needed to study the performance dependence of Deep-Interior on the noise configuration. The Deep-Interior network has not yet been trained to reduce noise. Noise will remain at low-dose settings. (3) Since there are no differentiation operations involved in the formation of the weighted backprojection image $B(\vec{x})$, one can expect that this new strategy may tolerate sparse view angle sampling better than other methods involving differentiation operations between view angles. This warrants another systematic investigation to pinpoint how the reconstruction performance depends on the view angle sampling conditions. (4) As shown in the paper, it is the specific definition of the weighted backprojection image $B(\vec{x})$ shown in Equation (7) that enables the reconstructed image $B(\vec{x})$ to be a blurred image of the corresponding image function $f(\vec{x})$ with a shift-invariant blurring kernel for any ROI sizes and the corresponding scan angular ranges satisfying the Tuy data sufficiency condition.

## 6 | CONCLUSION

A new interior tomographic reconstruction strategy was developed and validated by a weighted backprojection and deep learning steps referred to as Deep-Interior. This new strategy enables accurate image reconstructions for small ROIs with diameters larger than 5.0 cm with high quantitative reconstruction accuracy.

## ACKNOWLEDGMENTS

This work is partially supported by NIH grants R01HL153594, R01EB032474, and R01EB034011. One of the authors, G.H.C., received partial support from the WARF Named Professorship, a chaired professorship bestowed by the University of Wisconsin-Madison's Office of the Vice Chancellor for Research and Graduate Education, with funding from the Wisconsin Alumni Research Foundation (WARF). The authors would like to thank one of the anonymous reviewers for pointing out that the geometrical identity, Equation (C10), in Appendix C was also utilized by Dennerlein et al. in Ref. [46] to derive a fan-beam FBP reconstruction algorithm that does not incorporate a distance-dependent weighting factor in the backprojection step.

## CONFLICT OF INTEREST STATEMENT

The authors have no conflicts to disclose.

## DATA AVAILABILITY STATEMENT

The data that support the findings of this study are available from the corresponding author upon reasonable request.

## REFERENCES

1. Wang G, Yu H. The meaning of interior tomography. *Phys Med Biol*. 2013;58:R161.
2. Defrise M, Noo F, Clackdoyle R, Kudo H. Truncated Hilbert transform and image reconstruction from limited tomographic data. *Inverse Problems*. 2006;22:1037-1053.
3. Kudo H, Courdurier M, Noo F, Defrise M. Tiny a priori knowledge solves the interior problem. In: *IEEE Nuclear Science Symposium Conference Record*. Vol 6. 2007: 4068-4075.
4. Kudo H, Courdurier M, Noo F, Defrise M. Tiny a priori knowledge solves the interior problem in computed tomography. *Phys Med Biol*. 2008;53:2207-2231.
5. Ye Y, Yu H, Wei Y, Wang G. A general local reconstruction approach based on a truncated Hilbert transform. *Int J Biomed Imaging*. 2007(2007).
6. Courdurier M, Noo F, Defrise M, Kudo H. Solving the interior problem of computed tomography using a priori knowledge. *Inverse Problems*. 2008;24:065001.
7. Ye Y, Yu H, Wang G. Exact interior reconstruction with cone-beam CT. *Int J Biomed Imaging*. 2007;2007:10693.
8. Yu H, Ye Y, Wang G. Interior reconstruction using the truncated Hilbert transform via singular value decomposition. *J X Ray Sci Technol*. 2008;16:243-251.
9. Wang G, Yu H, Ye Y. A scheme for multisource interior tomography. *Med Phys*. 2009;36:3575-3581.
10. Taguchi K, Xu J, Srivastava S, Tsui BMW, Cammin J, Tang Q. Interior region-of-interest reconstruction using a small, nearly piecewise constant subregion. *Med Phys*. 2011;38:1307-1312.
11. Tang S, Yang Y, Tang X. Practical interior tomography with radial Hilbert filtering and a priori knowledge in a small round area. *J X Ray Sci Technol*. 2012;20:405-422.
12. Jin X, Katsevich A, Yu H, Wang G, Li L, Chen Z. Interior tomography with continuous singular value decomposition. *IEEE Trans Med Imaging*. 2012;31:2108-2119.
13. Lauzier PT, Qi Z, Zambelli J, Bevins N, Chen, G-H,. Interior tomography in x-ray differential phase contrast CT imaging. *Phys Med Biol*. 2012;57:N117.
14. Katsevich E, Katsevich A, Wang G. Stability of the interior problem with polynomial attenuation in the region of interest. *Inverse Problems*. 2012;28:065022.
15. Yu H, Wang G. Compressed sensing based interior tomography. *Phys Med Biol*. 2009;54:2791-2805.
16. Yu H, Yang J, Jiang M, Wang G. Supplemental analysis on compressed sensing based interior tomography. *Phys Med Biol*. 2009;54:N425-N432.
17. Han W, Yu H, Wang G. A general total variation minimization theorem for compressed sensing based on interior tomography. *Int J Biomed Imaging*. 2009 (2009).
18. Yang J, Yu H, Jiang M, Wang G. High order total variation minimization for interior tomography. *Inverse Problems*. 2010;26:350131-3501329.
19. Yang J, Cong W, Jiang M, Wang G. Theoretical study on high order interior tomography. *J X Ray Sci Technol*. 2012;20:423-436.
20. Ward JP, Lee M, Ye JC, Unser M. Interior tomography using a 1D generalized total variation. Part I: Mathematical foundation. *SIAM J Imag Sci*. 2015;8:226-247.
21. Lee M, Han Y, Ward, JP, Unser M, Ye, JC,. Interior tomography using a 1D generalized total variation. Part II: Multiscale implementation. *SIAM J Imag Sci*. 2015;8:2452-2486.
22. Chen, GH, Tang J, Leng S. Prior image constrained compressed sensing (PICCS): a method to accurately reconstruct dynamic CT images from highly undersampled projection data sets. *Med Phys*. 2008;35:660-663.
23. Lauzier PT, Tang J, Chen G-H. Time-resolved cardiac interventional cone-beam CT reconstruction from fully truncated projections using the prior image constrained compressed sensing (PICCS) algorithm. *Phys Med Biol*. 2012;57:2461-2476.
24. Zou Y, Pan X. Image reconstruction on PI-lines by use of filtered backprojection in helical cone-beam CT. *Phys Med Biol*. 2004;49:2717.
25. Zou Y, Pan X. Exact image reconstruction on PI-lines from minimum data in helical cone-beam CT. *Phys Med Biol*. 2004;49:941-959.
26. Pan X, Zou Y, Xia D. Image reconstruction in peripheral and central regions-of-interest and data redundancy. *Med Phys*. 2005;32:673-684.
27. Noo F, Clackdoyle R, Pack, JD,. A two-step Hilbert transform method for 2D image reconstruction. *Phys Med Biol*. 2004;49:3903.
28. Zhuang T, Leng S, Nett, BE, Chen, G-H,. Fan-beam and cone-beam image reconstruction via filtering the backprojection image of differentiated projection data. *Phys Med Biol*. 2004;49:5489.
29. Kolditz D, Kyriakou Y, Kalender WA. Volume-of-interest (VOI) imaging in C-arm flat-detector CT for high image quality at reduced dose. *Med Phys*. 2010;37:2719-2730.
30. Shen Y, Yi Y, Zhong Y, et al. High resolution dual detector volume-of-interest cone beam breast CT–Demonstration with a benchtop system. *Med Phys*. 2011;38:6429-6442.

31. Dennerlein F, Maier A. Approximate truncation robust computed tomography–ATRACT. *Phys Med Biol*. 2013;58:6133-6148.
32. Wang G, Ye JC, De Man B. Deep learning for tomographic image reconstruction. *Nat Mach Intell*. 2020;2:737-748.
33. Li Y, Li K, Zhang C, Montoya J, Chen G-H. Learning to reconstruct computed tomography images directly from sinogram data under a variety of data acquisition conditions. *IEEE Trans Med Imaging*. 2019;38:2469-2481.
34. Han Y, Ye JC. One network to solve all ROIs: Deep learning CT for any ROI using differentiated backprojection. *Med Phys*. 2019;46:e855-e872.
35. Han Y, Wu D, Kim K, Li Q. End-to-end deep learning for interior tomography with low-dose x-ray CT. *Phys Med Biol*. 2022;67:115001.
36. Huang Y, Preuhs A, Manhart M, Lauritsch G, Maier A. Data extrapolation from learned prior images for truncation correction in computed tomography. *IEEE Trans Med Imaging*. 2021;40:3042-3053.
37. Li M, Fang Z, Cong W, et al. Clinical micro-CT empowered by interior tomography, robotic scanning, and deep learning. *IEEE Access*. 2020;8:229018-229032.
38. Bates R. Towards improvements in tomography. *New Zealand J Sci*. 1971;14:883-896.
39. Barrett HH, Swindell W. *Radiological Imaging: The Theory of Image Formation, Detection, and Processing*. Academic Press; 1981.
40. Natterer F. *The Mathematics of Computerized Tomography*. SIAM; 2001.
41. Gullberg GT. The reconstruction of fan-beam data by filtering the back-projection. *Comput Graph Image Process*. 1979;10:30-47.
42. Tuy HK. An inversion formula for cone-beam reconstruction. *SIAM J Appl Math*. 1983;43:546-552.
43. Ge Y, Zhang Q, Hu Z, et al. Deconvolution-based backproject-Filter (BPF) computed tomography image reconstruction method using deep learning technique. arXiv preprint arXiv:1807.01833. 2018.
44. Ronneberger O, Fischer P, Brox T. U-net: Convolutional networks for biomedical image segmentation. In: *International Conference on Medical image computing and computer-assisted intervention*. Springer; 2015:234-241.
45. Feldkamp LA, Davis LC, Kress JW. Practical cone-beam algorithm. *Josa A*. 1984;1:612-619.
46. Dennerlein F, Noo F, Hornegger J, Lauritsch G. Fan-beam filtered-backprojection reconstruction without backprojection weight. *Phys Med Biol*. 2007;52:3227.

**How to cite this article:** Zhang C, Chen G-H. Deep-Interior: A new pathway to interior tomographic image reconstruction via a weighted backprojection and deep learning. *Med Phys*. 2024;51:946–963.
https://doi.org/10.1002/mp.16880

## APPENDIX A: PROOF OF THE CENTRAL THEOREM

In this appendix, we present a proof of the central theorem as shown in Equation (11) with $B(\vec{x})$ defined in Equation (7).

It is instructive to start the proof by writing the backprojection image $B(\vec{x})$ in terms of parameterization $(\rho,\theta)$ as that in a parallel-beam geometry.

$$\begin{aligned} B(\vec{x}) &= \int_0^{\pi} d\theta P(\rho,\theta)|_{\rho=\vec{x}\cdot\hat{n}}, \\ &= \int_0^{\pi} d\theta \int_{-\infty}^{+\infty} d\rho P(\rho,\theta)\delta(\rho-\vec{x}\cdot\hat{n}). \end{aligned} \tag{A1}$$

where $\hat{n}=(\cos\theta,\sin\theta)$ is a unit vector and $\delta(\cdot)$ is the Dirac $\delta$–function in the sense of distributions. Using the line integral definition shown in Equation (1) to replace $P(\rho,\theta)$ in above equation, one obtains,

$$B(x,y) = \iint_{D} dx'dy' f(x',y') \frac{I(\vec{x}',\vec{x})}{||\vec{x}'-\vec{x}||}, \tag{A2}$$

where $||\vec{x}'-\vec{x}||$ is the Euclidean distance between two points $\vec{x}$ and $\vec{x}'$ and the function $I(\vec{x}',\vec{x})$ is defined as follows:

$$\begin{aligned} I(\vec{x}',\vec{x}) &= \int_0^{\pi} d\theta \int_{-\infty}^{\infty} d\rho ||\vec{x}'-\vec{x}||\delta(\rho-\vec{x}\cdot\hat{n})\delta(\rho-\vec{x}'\cdot\hat{n}) \\ &= \int_0^{\pi} d\theta \int_{-\infty}^{\infty} d\rho ||\vec{x}'-\vec{x}||\delta[(\vec{x}-\vec{x}')\cdot\hat{n}]\delta(\rho-\vec{x}\cdot\hat{n}) \\ &= \int_0^{\pi} d\theta \int_{-\infty}^{\infty} d\rho \delta\left[\frac{(\vec{x}-\vec{x}')}{||\vec{x}'-\vec{x}||}\cdot\hat{n}\right]\delta(\rho-\vec{x}\cdot\hat{n}) \\ &= \int_0^{\pi} d\theta \int_{-\infty}^{\infty} d\rho \delta[\cos(\theta-\theta_0(\vec{x},\vec{x}'))]\delta(\rho-\vec{x}\cdot\hat{n}), \end{aligned} \tag{A3}$$

where the angle $\theta_0(\vec{x},\vec{x}')$ is defined as follows,

$$\tan\theta_0(\vec{x},\vec{x}') = \frac{y-y'}{x-x'} \tag{A4}$$

In next step, we change variable from $(\rho,\theta)$ back to the fan-beam parameterization $(t,\gamma)$ with a curved detector in Equation (A1) to obtain the following result:

$$B(\vec{x}) = \int_0^{\Gamma} dt \int_{-\frac{\gamma_m}{2}}^{\frac{\gamma_m}{2}} d\gamma R\cos\gamma\,\omega(t,\gamma) g_m(t,\gamma)|_{\rho=\vec{x}\cdot\hat{n}}. \tag{A5}$$

Here the factor $R\cos\gamma$ is the Jacobian factor. To account for the potential data redundancy in fan-beam acquisitions with an angular range of $\Gamma$, a normalized weighting factor $\omega(t,\gamma)$ is also introduced since this data redundancy is not present in the corresponding parallel-beam parameterization in terms of $(\rho,\theta)$ in Equation (A1). Using the transform shown in Equation (2) for the constraint $\rho=\vec{x}\cdot\hat{n}$, we obtain the following result:

$$B(\vec{x}) = \int_0^{\Gamma} dt \int_{-\frac{\gamma_m}{2}}^{\frac{\gamma_m}{2}} d\gamma R\cos\gamma\,\omega(t,\gamma) g_m(t,\gamma)\delta(\rho-\vec{x}\cdot\hat{n}),$$

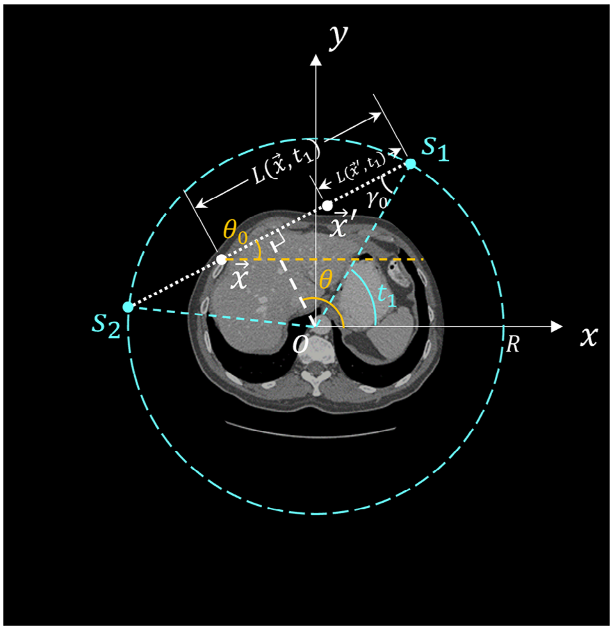

**FIGURE A1** The geometry used in the proof of the central theorem.

$$= \int_0^\Gamma dt \frac{R\cos\gamma\,\omega(t,\gamma)}{L(\vec{x},t)} g_m(t,\gamma)|_{\gamma=\gamma_0(\vec{x},t)}, \tag{A6}$$

where we used the following identity:

$$\delta(\rho - \vec{x}\cdot\hat{n}) = \delta[L(\vec{x},t)\sin(\gamma - \gamma_0(\vec{x},t))]. \tag{A7}$$

Equation (A6) is nothing but Equation (7) in the main text.

Similarly, the factor $I(\vec{x}', \vec{x})$ defined in Equation (A3) can be calculated in fan-beam geometry with a curved detector as follows.

$$\begin{aligned}
I(\vec{x}', \vec{x}) &= \int_0^\pi d\theta \int_{-\infty}^{\infty} d\rho\,\delta[\cos(\theta - \theta_0(\vec{x}, \vec{x}'))]\delta(\rho - \vec{x}\cdot\hat{n}),\\
&= \int_0^\Gamma dt \int_{-\frac{\gamma_m}{2}}^{\frac{\gamma_m}{2}} d\gamma R\cos\gamma\,\omega(t,\gamma)\delta\left[\cos\left(t + \frac{\pi}{2} + \gamma - \theta_0(\vec{x}, \vec{x}')\right)\right]\\
&\times \delta[L(\vec{x},t)\sin(\gamma - \gamma_0(\vec{x},t))]\\
&= R\int_0^\Gamma dt \frac{\omega(t,\gamma)}{L(\vec{x},t)}\cos\gamma_0(\vec{x},t)\delta\left[\cos\left(t + \gamma_0(\vec{x},t) + \frac{\pi}{2} - \theta_0(\vec{x}, \vec{x}')\right)\right]\\
&= \int_0^\Gamma dt \frac{R\cos\gamma_0(\vec{x},t)\omega(t,\gamma)}{L(\vec{x},t)}\delta[g(t)],
\end{aligned} \tag{A8}$$

where function $g(t)$ is defined as follows:

$$g(t) = \sin[t + \gamma_0(\vec{x},t) - \theta_0(\vec{x}, \vec{x}')]. \tag{A9}$$

To gain insight into the solution of $g(t) = 0$, with the help of Figure A1, we find the following facts are beneficial: Given two points $\vec{x} = (x, y)$ and $\vec{x}' = (x', y')$ in the scanning field of view. The straight line passing through these two points intersects the scanning trajectory at two source locations $S_1 = (R\cos t_1, R\sin t_1)$ and $S_2 = (R\cos t_2, R\sin t_2)$. If we denote the azimuthal angle of the vector $\Delta\vec{x} = \vec{x}' - \vec{x}$ as $\theta_0(\vec{x}, \vec{x}')$ and $\gamma_0(\vec{x}, t) = \arctan\frac{x\sin t - y\cos t}{R - x\cos t - y\sin t}$ the angle from iso-ray to the image point $\vec{x}$ when it is viewed from the source location $(R\cos t, R\sin t)$, then we have the following inequality $t + \gamma_0(\vec{x}, t) \geq \theta_0(\vec{x}, \vec{x}')$ with equality taken at $t = t_1$ or $t = t_2$. As a result, the final integral in Equation (A8) can be readily evaluated at these two source locations $t = t_1$ or $t = t_2$ to obtain the following results:

$$\begin{aligned}
I(\vec{x}', \vec{x}) = |&\frac{R\cos\gamma_0(\vec{x},t_1)\omega(\gamma_0,t_1)}{L(\vec{x},t_1)\left(1 + \frac{\partial}{\partial t}\gamma_0(\vec{x},t)|_{t=t_1}\right)}\\
&+ \frac{R\cos\gamma_0(\vec{x},t_2)\omega(\gamma_0,t_2)}{L(\vec{x},t_2)\left(1 + \frac{\partial}{\partial t}\gamma_0(\vec{x},t)|_{t=t_2}\right)}|.
\end{aligned} \tag{A10}$$

To proceed to the final result, we will need to use the following crucial identity (Appendix B):

$$L(\vec{x},t)\left(1 + \frac{\partial}{\partial t}\gamma_0(\vec{x},t)\right) \equiv R\cos\gamma_0(\vec{x},t). \tag{A11}$$

As a result of the above identity, Equation (A10) is readily evaluated to be

$$I(\vec{x}', \vec{x}) = \omega(\gamma_0, t_1) + \omega(\gamma_0, t_2) \equiv 1 \tag{A12}$$

Substituting this result back in Equation (A2), we conclude

$$B(\vec{x}) = \iint_D dx'dy' \frac{f(\vec{x}')}{||\vec{x}' - \vec{x}||} = f(\vec{x}) \circledast \frac{1}{||\vec{x}||}. \tag{A13}$$

This completes the proof of the main theorem.

## APPENDIX B: PROOF OF THE IDENTITY IN EQUATION (A11)

In this appendix, we prove the identity shown in Equation (A11). Using the definition of $\gamma_0(\vec{x}, t)$, some straightforward algebraic calculations yield:

$$\begin{aligned}
1 + \frac{\partial}{\partial t}\gamma_0(\vec{x},t) &= 1 + \frac{R(x\cos t + y\sin t) - x^2 - y^2}{L^2(\vec{x},t)},\\
&= 1 + \frac{R\vec{x}\cdot\hat{n}(t) - ||\vec{x}||^2}{L^2(\vec{x},t)},\\
&= \frac{L^2(\vec{x},t) - ||\vec{x}||^2 + R\vec{x}\cdot\hat{n}(t)}{L^2(\vec{x},t)}.
\end{aligned} \tag{B1}$$

Here $\hat{n}(t) = (\cos t, \sin t)$ is a unit vector and $||\vec{x}||$ is the Euclidean norm of the vector $\vec{x}$. By drawing a perpendicular line from point $\vec{x}$ to the iso-ray, one can immediately see the following identity using the Pythagoras theorem:

$$L^2(\vec{x},t) - [R - \vec{x}\cdot\hat{n}(t)]^2 = ||\vec{x}||^2 - [\vec{x}\cdot\hat{n}(t)]^2, \tag{B2}$$

that is, $L^2(\vec{x},t) - ||\vec{x}||^2 = [R - \vec{x}\cdot\hat{n}(t)]^2 - [\vec{x}\cdot\hat{n}(t)]^2$. After we substitute this identity into Equation (B1), we obtain the following equation:

$$\begin{aligned} 1 &+ \frac{\partial}{\partial t}\gamma_0(\vec{x},t) \\ &= \left(\frac{R - \vec{x}\cdot\hat{n}(t)}{L(\vec{x},t)}\right)^2 + \frac{R - \vec{x}\cdot\hat{n}(t)}{L(\vec{x},t)}\cdot\frac{R - [R - \vec{x}\cdot\hat{n}(t)]}{L(\vec{x},t)} \\ &= \cos^2\gamma_0(\vec{x},t) + \cos\gamma_0(\vec{x},t)\left[\frac{R}{L(\vec{x},t)} - \cos\gamma_0(\vec{x},t)\right], \\ &= \frac{R\cos\gamma_0(\vec{x},t)}{L(\vec{x},t)}. \end{aligned} \tag{B3}$$

This completes the proof of the identity shown in Equation (A11).

## APPENDIX C: BACKPROJECTION IMAGE USING UN-WEIGHTED BACKPROJECTION AT $\Gamma = 2\pi$

In this appendix, we show that a direct backprojection of fan-beam projection data without the proposed weighting scheme in Equation (7) can also yield a blurred backprojection image, that is, $f(\vec{x}) \circledast \frac{1}{||\vec{x}||}$, provided that the scan angular range $\Gamma = 2\pi$. By definition, the backprojection image $B_{2\pi}(\vec{x})$ is generated as follows:

$$\begin{aligned} B_{2\pi}(\vec{x}) &= \frac{1}{2}\int_0^{2\pi} dt g_m(\gamma)|_{\gamma=\gamma_0(\vec{x},t)}, \\ &= \frac{1}{2}\int_0^{2\pi} dt g_m(t,\gamma)\delta[\gamma - \gamma_0(\vec{x},t)], \end{aligned} \tag{C1}$$

where the factor of $\frac{1}{2}$ is introduced to account for the two-fold data redundancy in full scan acquisitions. Note that the line integral value $g_m(t,\gamma)$ is measured along the straight line $\ell$ parameterized by two parameters $(t,\gamma)$ which can also be parameterized by $(\rho,\theta)$ as follows:

$$\begin{aligned} g_m(t,\gamma) &= \iint_{\mathcal{D}} dxdy f(x,y)\delta(x\cos\theta + y\sin\theta - \rho), \\ &= \iint_{\mathcal{D}} dxdy f(x,y)\delta[L(\vec{x},t)sin(\gamma - \gamma_0(\vec{x},t))], \end{aligned} \tag{C2}$$

where Equation (A7) is used in the second line. Substituting the above equation back to Equation (C1), one gets

$$\begin{aligned} B_{2\pi}(\vec{x}) &= \frac{1}{2}\iint_{\mathcal{D}} dx'dy' f(x',y')\int_0^{2\pi} dt \\ &\times \delta[L(\vec{x}',t)sin(\gamma - \gamma_0(\vec{x}',t))]\delta[\gamma - \gamma_0(\vec{x},t)], \\ &= \frac{1}{2}\iint_{\mathcal{D}} dx'dy' f(x',y')\int_0^{2\pi} dt \\ &\times \delta[L(\vec{x}',t)\sin(\gamma_0(\vec{x},t) - \gamma_0(\vec{x}',t))], \\ &= \frac{1}{2}\iint_{\mathcal{D}} dx'dy' f(x',y') \\ &\times \left[\frac{1}{L(\vec{x}',t_1)}\frac{1}{|\frac{\partial}{\partial t}h(\vec{x},\vec{x}';t_1)|} + \frac{1}{L(\vec{x}',t_1)}\frac{1}{|\frac{\partial}{\partial t}h(\vec{x},\vec{x}';t_2)|}\right], \end{aligned} \tag{C3}$$

where $t_{1,2}$ are the two solutions of equation $h(\vec{x},\vec{x}';t) = \sin[\gamma_0(\vec{x},t) - \gamma_0(\vec{x}',t)] = 0$. This occurs at $\gamma_0(\vec{x},t) = \gamma_0(\vec{x}',t)$. Geometrically, this means that the two solutions are determined by the two intersections of the straight line connecting two points $\vec{x}$ and $\vec{x}'$ at the source trajectory. As a result, we have the following results:

$$\begin{aligned} &\frac{\partial}{\partial t}h(\vec{x},\vec{x}';t) \\ &= \cos[\gamma_0(\vec{x},t) - \gamma_0(\vec{x}',t)]\left[\frac{\partial}{\partial t}\gamma_0(\vec{x},t) - \frac{\partial}{\partial t}\gamma_0(\vec{x}',t)\right], \\ &= \frac{\partial}{\partial t}\gamma_0(\vec{x},t) - \frac{\partial}{\partial t}\gamma_0(\vec{x}',t), \\ &= \frac{R\cos\gamma_0(\vec{x},t)}{L(\vec{x},t)} - \frac{R\cos\gamma_0(\vec{x}',t)}{L(\vec{x}',t)}. \end{aligned} \tag{C4}$$

The identity Equation (B3) was used in the last equality. In other words, we have the following results:

$$\begin{aligned} L(\vec{x},t)|\frac{\partial}{\partial t}h(\vec{x},\vec{x}';t)| &= R\cos\gamma_0(\vec{x},t)\frac{|L(\vec{x}',t) - L(\vec{x},t)|}{L(\vec{x}',t)}, \\ &= R\cos\gamma_0(\vec{x},t)\frac{||\vec{x} - \vec{x}'||}{L(\vec{x}',t)}, \end{aligned} \tag{C5}$$

where we have used the following fact:

$$|L(\vec{x}',t) - L(\vec{x},t)| = ||\vec{x} - \vec{x}'||. \tag{C6}$$

In other words, Equation (C5) can now be written as

$$\frac{1}{L(\vec{x}',t)}\frac{1}{|\frac{\partial}{\partial t}h(\vec{x},\vec{x}';t)|} = \frac{L(\vec{x}',t)}{R\cos\gamma_0(\vec{x},t)||\vec{x} - \vec{x}'||}. \tag{C7}$$

Substituting the above result in Equation (C3), we obtain

$$B_{2\pi}(\vec{x}) = \frac{1}{2}\iint_{\mathcal{D}} dx'dy' f(x',y')\frac{1}{||\vec{x} - \vec{x}'||} \tag{C8}$$

$$\times\left[\frac{L(\vec{x}',t_1)}{R\cos\gamma_0(\vec{x},t_1)}+\frac{L(\vec{x}',t_2)}{R\cos\gamma_0(\vec{x},t_2)}\right].$$

Note also that

$$\begin{aligned}R\cos\gamma_0(\vec{x},t_2)&=R\cos\gamma_0(\vec{x},t_1),\\&=\frac{1}{2}[L(\vec{x}',t_1)+L(\vec{x}',t_2)],\end{aligned}\tag{C9}$$

at two source locations $t_{1,2}$ determined by $h(\vec{x},\vec{x}';t)=0$ as discussed before. We come to a the following result:

$$\begin{aligned}&\frac{L(\vec{x}',t_1)}{R\cos\gamma_0(\vec{x},t_1)}+\frac{L(\vec{x}',t_2)}{R\cos\gamma_0(\vec{x},t_2)},\\&=\frac{L(\vec{x}',t_1)+L(\vec{x}',t_2)}{R\cos\gamma_0(\vec{x},t_1)},\\&\equiv 2.\end{aligned}\tag{C10}$$

Note that this remarkable geometric identity requires contributions from two source locations, $t_1$ and $t_2$. Consequently, it is applicable only in the case of full-scan data acquisitions. Using this identity, we have reproduced the following elegant result,

$$B_{2\pi}(\vec{x})=\iint_{\mathcal{D}}dx'dy'f(x',y')\frac{1}{||\vec{x}-\vec{x}'||}=f(\vec{x})\circledast\frac{1}{||\vec{x}||},\tag{C11}$$

as first obtained by Gullberg[41] back in 1979. However, as shown in this appendix, the above result relies on the miraculous identity shown in Equation (C10), which is only valid for the full scan case. It is also worth noting that this identity was also used by Dennerlein et al. in Ref. [46] to derive a FBP reconstruction algorithm that does not include a distance-dependent weighting factor in the backprojection step. In contrast, when the backprojection image is defined as the one in Equation (A6) in Appendix A, that is, Equation (7) in the main text, then the above result is valid for any angular range satisfying the Tuy data sufficiency condition.